JACS
JOURNAL OF THE AMERICAN CHEMICAL SOCIETY
Article
pubs.acs.org/JACS

Photochemical Water Oxidation by Crystalline Polymorphs of Manganese Oxides: Structural Requirements for Catalysis

David M. Robinson, Yong Bok Go, Michelle Mui, Graeme Gardner, Zhijuan Zhang, Daniel Mastrogiovanni, Eric Garfunkel, Jing Li, Martha Greenblatt,* and G. Charles Dismukes*

Department of Chemistry and Chemical Biology, Rutgers, The State University of New Jersey, Piscataway, New Jersey 08854, United States

Supporting Information

ABSTRACT: Manganese oxides occur naturally as minerals in at least 30 different crystal structures, providing a rigorous test system to explore the significance of atomic positions on the catalytic efficiency of water oxidation. In this study, we chose to systematically compare eight synthetic oxide structures containing Mn(III) and Mn(IV) only, with particular emphasis on the five known structural polymorphs of MnO_2. We have adapted literature synthesis methods to obtain pure polymorphs and validated their homogeneity and crystallinity by powder X-ray diffraction and both transmission and scanning electron microscopies. Measurement of water oxidation rate by oxygen evolution in aqueous solution was conducted with dispersed nanoparticulate manganese oxides and a standard ruthenium dye photo-oxidant system. No Ru was absorbed on the catalyst surface as observed by XPS and EDX. The post reaction atomic structure was completely preserved with no amorphization, as observed by HRTEM. Catalytic activities, normalized to surface area (BET), decrease in the series Mn_2O_3 > Mn_3O_4 ≫ λ-MnO_2, where the latter is derived from spinel $LiMn_2O_4$ following partial Li^+ removal. No catalytic activity is observed from $LiMn_2O_4$ and four of the MnO_2 polymorphs, in contrast to some literature reports with polydispersed manganese oxides and electro-deposited films. Catalytic activity within the eight examined Mn oxides was found exclusively for (distorted) cubic phases, Mn_2O_3 (bixbyite), Mn_3O_4 (hausmannite), and λ-MnO_2 (spinel), all containing Mn(III) possessing longer Mn−O bonds between edge-sharing MnO_6 octahedra. Electronically degenerate Mn(III) has antibonding electronic configuration e_g^1 which imparts lattice distortions due to the Jahn−Teller effect that are hypothesized to contribute to structural flexibility important for catalytic turnover in water oxidation at the surface.

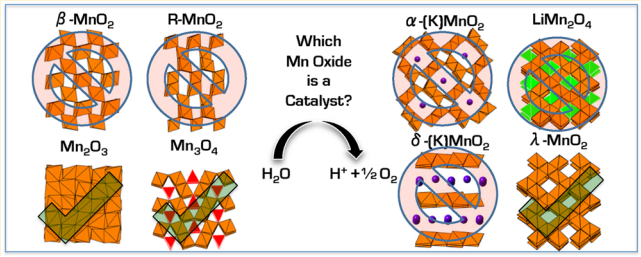

INTRODUCTION

Development of commercial energy storage systems based on water electrolysis to H_2 and O_2 is limited by availability of low-cost, earth-abundant electro-catalysts needed to overcome the activation energy barriers above the minimum thermodynamic potential (1.23 V vs SHE). Commercial water electrolyzers are typically limited by the oxidation reaction at the anode (OER, O_2 evolving reaction) and consequently use supported precious metals, commonly Pt, RuO_2, and IrO_2, which have the lowest energy losses.[1]

Bulk metal oxides have long been of interest as heterogeneous water oxidation catalysts, with multiple surveys documenting relative activities of polydispersed compositions and disordered structure types.[2−4] Among these, the precious metal oxides like RuO_2 and IrO_2 were found to be highly active,[2,5] but owing to high cost and low natural abundance, these are not considered globally scalable. Among the catalytically more active nonprecious metal oxides are nanocrystalline spinels, mainly composed of manganese[6] or cobalt,[7,8] and perovskites with diverse components including cobalt, nickel and lanthanum.[9] Catalysis of water oxidation by nanocrystals of spinel Co_3O_4 and $NiCo_2O_4$ can occur more efficiently upon either incorporation into mesoporous silica substrates that may serve as possible proton transfer sites, or as electro-catalysts by coupling to electrodes.[8,10,11]

Identification of the catalytic site within spinels was aided by use of binary spinels, AB_2O_4, possessing labile "A site" cations. The spinel λ-MnO_2 obtained by delithiation of spinel $LiMn_2O_4$ becomes active in water oxidation only following removal of Li^+.[6] The catalytic activity was attributed to the "B site" cations which are arranged in Mn_4O_4 cubes that become more flexible upon "A site" removal. The importance of the M_4O_4 topology for water oxidation was further established by activity observed from two molecular cubanes compriing M = Mn or Co.[12,13]

The difficulty of controlling which of multiple polymorphs of any given metal oxide forms under the synthesis conditions has often been overlooked in accounting for the wide range of catalytic activities reported for compositionally identical materials. For example, among the two stoichiometrically identical polymorphs of nanocrystalline $LiCoO_2$, only the cubic phase (with Co_4O_4 units) is catalytically active in water

Received: October 18, 2012
Published: February 7, 2013

   dx.doi.org/10.1021/ja310286h | J. Am. Chem. Soc. 2013, 135, 3494−3501

oxidation, while the layered phase (with Co_3LiO_4 units) is inert.[7]

Electro-oxidation of solutions of manganese and cobalt salts at ambient temperature also forms metal oxides, typically polydispersed and structurally disordered. Among these materials, cobalt(II) phosphate solutions have been known for decades to form an oxide layer upon electro-oxidation[14,15] or chemical oxidation[16] that are effective water oxidation catalysts. These materials have been reexamined recently with renewed interest.[17] Catalytic activity has been observed from manganese oxide nanoparticles synthesized within a mesoporous crystalline silica substrate.[18] Although these Mn nanophases lack long-range crystal order, XANES spectroscopy suggests a composition similar to that of Mn_2O_3 and Mn_3O_4. The water oxidation activity of amorphous manganese oxides has been attributed to higher mobility of oxygen atoms within the disordered lattice.[19] Through electrical cycling, a more active disordered manganese oxide layer can be deposited on electrodes.[20] Polydispersed, noncrystalline $CaMn_2O_4{\cdot}H_2O$ has also been found to exhibit water oxidation activity.[21]

The challenge in deciphering the source of catalytic activity of these disordered materials stems in part from the large range of possible polymorphs that have been found (or can exist) for each material. For example, minerals of manganese oxides/hydroxides occur naturally in 30 different crystal structures in a range of manganese oxidation states.[22] Some of these manganese oxide polymorphs have been tested for water oxidation activity, but only few comparatively. Nanoparticles of α-MnO_2, β-MnO_2 and Mn_2O_3 have all been reported to catalyze water oxidation when used in a photooxidant system.[19,21,23] Electrodeposited δ-MnO_2 particles on electrodes were found to oxidize water, but only under strongly alkaline conditions.[24] As noted earlier, nanocrystals of another polymorph, λ-MnO_2, are active catalytically, but its isostructural precursor, $LiMn_2O_4$, has no activity.[6]

To further resolve the source of catalytic activity and understand the structural and physicochemical basis of catalysis, we compared eight different nanocrystalline manganese oxides all synthesized and characterized both compositionally and structurally to uniform standards in our laboratory (Figure 1).

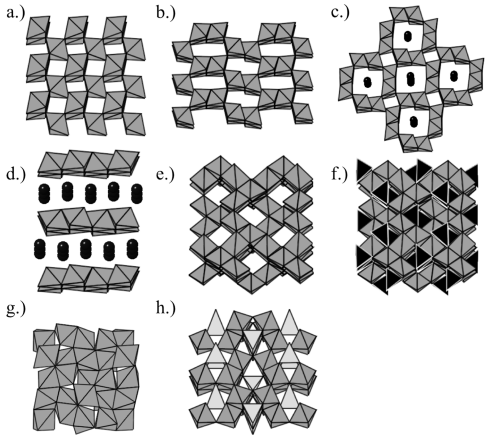

Figure 1. Polyhedral representation of the eight Mn oxides reported herein: (a) β-MnO_2, (b) R-MnO_2, (c) α-MnO_2, (d) δ-MnO_2, (e) λ-MnO_2, (f) $LiMn_2O_4$, (g) Mn_2O_3, and (h) Mn_3O_4. The light, dark, and black polyhedra represent Mn^{2+} tetrahedra, Mn^{3+} and Mn4+ octahedra, and Li^{1+} tetrahedra, respectively. Black spheres represent K^+ ions.

In our study, we chose to focus on structures with Mn(III) and Mn(IV) oxidation states, with particular emphasis on the five primary polymorphs of MnO_2. In this work, we also examine untested polymorphs of manganese oxide.

EXPERIMENTAL SECTION

Synthesis of β-MnO_2 (a). Synthesis as described in ref 25 yielded a mixture of α- and β-MnO_2. In our work, replacing $(NH_4)_2S_2O_8$ with $Na_2S_2O_8$ resulted in majority β-MnO_2. An aqueous solution of $MnSO_4$ (8 mmol) and $Na_2S_2O_8$ (8 mmol) was heated in a stainless steel reactor with a Teflon liner at 120 °C for 12 h. The resulting product was centrifuged, decanted and washed with deionized H_2O and dried at 90 °C in air. However, the resulting product contained some Mn_2O_3 impurity and was further purified with an additional hydrothermal procedure (Supporting Information).

Synthesis of R-MnO_2 (b). (Adapted from Russouw et al.[26] with increased temperature for higher purity samples) $LiMn_2O_4$ powder (f) was added to a 3 M H_2SO_4 solution (100 mg: 50 mL) to form an aqueous suspension and refluxed in an oil bath at 120 °C for 28 h. The solution was centrifuged, decanted and washed with bicarbonate solution and deionized H_2O and dried at 90 °C in air to form nanocrystalline R-MnO_2.

Synthesis of α-MnO_2 (c).[27] An aqueous solution of Mn$(OAc)_2{\cdot}4H_2O$ (5 mmol) was transferred into a solution of $KMnO_4$ (10 mmol). The reaction mixture was stirred at room temperature overnight and the resulting product was centrifuged, decanted and washed with deionized H_2O and dried at 100 °C overnight to form nanocrystalline α-MnO_2. An alternative synthesis of the K^+ free α-MnO_2 is described in the Supporting Information.

Synthesis of δ-MnO_2 (d).[28] An aqueous solution of 0.38 M $KMnO_4$ was added to a 1.4 M glucose solution. As the resulting brown gel undergoes syneresis, the water is decanted and the product was dried at 110 °C for 24 h. The resulting xerogel was then calcined at 400 °C, followed by washing with deionized H_2O and drying at 90 °C in air to form nanocrystalline potassium type δ-MnO_2.

Synthesis of λ-MnO_2 (e). Nanocrystalline $LiMn_2O_4$ powder (f) was added to a 0.1 M HNO_3 solution (100 mg: 10 mL) to form an aqueous suspension. After 2 h of sonication, the solution was centrifuged, decanted and washed with bicarbonate solution and deionized H_2O and dried at 90 °C in air to form nanocrystalline λ-MnO_2.

Synthesis of $LiMn_2O_4$ (f).[6] An aqueous solution of Mn$(OAc)_2{\cdot}4H_2O$ (5.0 mmol) and $LiNO_3$ (2.5 mmol) was mixed with an aqueous solution of citric acid (15 mmol) and urea (15 mmol). Concentrated nitric acid was added to the starting solution in the volume ratio of 1:0.1. The solution was evaporated at 80 °C for 4−6 h with continuous stirring to remove the water. The resulting resin was dried at 170 °C for 12 h. The sponge-like resin was calcined at 350 °C for 12 h to yield nanocrystalline $LiMn_2O_4$.

Synthesis of Mn_2O_3 (g). (Adapted from Lei et al.[29] with $MnCO_3$ pretreatment for smaller particle size) $MnCO_3$ powder (500 mg) was dissolved in a dilute HCl solution and was heated in a stainless steel reactor with a Teflon liner at 150 °C for 10 h. The product was washed with bicarbonate solution and dried at 100 °C overnight followed by calcination at 550 °C for 4 h to form nanocrystalline Mn_2O_3.

Synthesis of Mn_3O_4 (h).[30,31] An 80% hydrazine solution (5 mL) was added dropwise to an aqueous solution of 0.2 M $KMnO_4$ forming a brown precipitate and gaseous byproducts. The solution was stirred at room temperature for 12 h. The solid product was centrifuged, decanted and washed with deionized H_2O and dried at 100 °C overnight to form nanocrystalline Mn_3O_4.

All the reactants were reagent grade and used as purchased without further purification. Particle morphologies and sizes were observed by scanning electron microscopy (Zeiss Sigma Field Emission SEM with Oxford EDSLEO FESEM). The powder X-ray diffraction patterns (PXD) of the sample powders were collected on a Bruker D8 Advance diffractometer (Bragg−Brentano geometry, Cu Kα radiation) and BET surface area was measured by Quantachrome Autosorb porosity analyzer. Post reaction crystallinity was determined using high-

dx.doi.org/10.1021/ja310286h | J. Am. Chem. Soc. 2013, 135, 3494−3501

resolution transmission electron microscopy (Phillips CM200 FEG-TEM) with energy dispersive X-ray spectroscopy (PGT-IMIX EDX) capabilities. EDX and X-ray photoelectron spectroscopy (Thermo-scientific K-alpha XPS) were used to measure Ru decomposition and metal impurities. A widely adopted photo-oxidant assay was used to quantify water oxidation rate as O_2 evolution.[2,6,7,18,23] This assay uses a solution of 5×10^{-4} M $Ru(bpy)_3Cl_2 \cdot 6H_2O$ and 1.0×10^{-2} M $Na_2S_2O_8$ in a bicarbonate buffer (0.1 mM) poised at pH 7.0 (adjusted with H_2SO_4). Catalyst suspensions tested were ~250 ppm and were sonicated for 10 min before measurements. The chamber was illuminated with a mercury arc lamp with filters for UV (395 nm cutoff filter) and IR ($CuSO_4$ solution) at a light intensity of 4.3 mW/cm^2 measured by a Newport power meter (Figure S1). Dissolved O_2 concentrations were measured with a Clark type electrode (Hansatek Ltd.), which was calibrated with both sodium dithionate and N_2 purged solutions. Gaseous O_2 was assayed on a GOW MAC Series 350 Gas Chromatograph (GC) with a thermal conductivity detector.

The postreaction particles used in HRTEM and XPS were washed and centrifuged for isolation and analysis without sonication or pH treatment to prevent particle modification. 4x higher catalyst concentration was used for O_2 assays to allow for higher postreaction yield.

RESULTS

Within the five MnO_2 polymorphs, the structural variations are the result of bonding motifs of the basic MnO_6 octahedral unit. β-MnO_2 (Pyrosulite) adopts rutile structure, where columns of edge sharing MnO_6 octahedra are corner-shared with an adjacent chain generating one-dimensional channel along the c-axis (Figure 1a). R-MnO_2 (Ramsdellite) and α-MnO_2 (Cryptomelane-type) are extensions of the β structure: chains of edge sharing double octahedra are corner-shared with adjacent chains creating (1×2) and (2×2) channels along the c-axis, respectively (Figure 1b,c). While given distinct nomenclature, γ-MnO_2 (Nsutite), a naturally occurring mineral, and ε-MnO_2 are structurally defined as mixtures containing the repeating units of both β-MnO_2 and R-MnO_2.[32] These materials have a nonspecific ratio of the two structural components and provide an ambiguous library standard for diffraction patterns. As a result, neither γ-MnO_2 nor ε-MnO_2 were pursued in our study. The δ-MnO_2 (Birnessite-type) is a synthetically defined layered polymorph with repeating single layers of MnO_2 separated by alkali cations and/or H_2O with distinct interlayer separations (Figure 1d). The individual MnO_2 layers are comprised of edge-shared MnO_6 octahedra. The final polymorph, λ-MnO_2, is not a naturally occurring structure (Figure 1e) but was discovered as a byproduct of lithium cycling of $LiMn_2O_4$ (Figure 1f) battery materials.[33] Upon exhaustive delithiation (>90% tetrahedral A site vacancies), the spinel framework of $LiMn_2O_4$ is retained in λ-MnO_2.[6]

Among the three remaining manganese oxides, only a single structural polymorph is accessible for each stoichiometry (Figure 1f, $LiMn_2O_4$; Figure 1g, Mn_2O_3 (bixbyite); Figure 1h, Mn_3O_4). The battery cathode material, $LiMn_2O_4$, is a well-defined binary AB_2O_4 spinel with tetrahedral A site cations and octahedral B site cations. Mn_3O_4 (Hausmannite) is a distorted spinel structure containing Mn^{2+} in the tetrahedral sites and Mn^{3+} in octahedral sites. Despite claims for a second phase of Mn_2O_3 in the literature, the existence of a distinct γ-Mn_2O_3 has no definitive evidence and is most likely mislabeled Mn_3O_4 (identical PXD patterns). The structure of Mn_2O_3 is derived from anion deficient cubic fluorite with two types of edge sharing groups of distorted MnO_6 octahedra.

Unique PXD patterns verify the formation of the Mn oxide phases we synthesized. Identification and purity were established by comparison to database[34] and primary literature reports.[6,25−30] The PXD pattern for β-MnO_2 (Figure 2a)

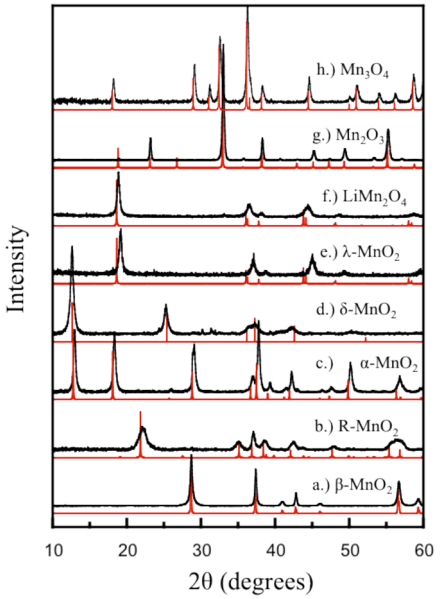

Figure 2. Powder X-ray diffraction patterns of the eight Mn oxides reported herein: (a) β-MnO_2, (b) R-MnO_2, (c) α-MnO_2, (d) δ-MnO_2, (e) λ-MnO_2, (f) $LiMn_2O_4$, (g) Mn_2O_3, and (h) Mn_3O_4. The sample patterns (black) agree with the reference (red) in all cases except (e) where the reference shown is for $LiMn_2O_4$ and the observed shift is indicative of delithiation forming λ-MnO_2.

reveals a highly stable rutile structure and R-MnO_2 (Figure 2b) contains a definitive pattern for the rarely isolated, pure polymorph. But within the remaining MnO_2 polymorphs, there is further complexity in the occupancy of various cation sites that minimally affect the crystal structure. Three polymorphs, α-MnO_2 (Figure 2c), δ-MnO_2 (Figure 2d), and λ-MnO_2 (Figure 2e), contain sites within the structures for monovalent cations.

Either K^+, Na^+ and/or H_2O are most commonly found occupying the sites within the (2×2) channel of α-MnO_2 (a rare 3×3 mineral structures exist with divalent cations) and the layered structure of δ-MnO_2. The term cryptomelane used earlier refers specifically to the K^+ type α-MnO_2 that is synthesized herein. Additionally, α-MnO_2 without K^+ cation was synthesized and tested for comparison with identical results (Supporting Information). However, PXD is unable to determine the occupancy of these cation sites within α-MnO_2 as a result of the lack of spatial confinement for these atoms. The layered δ-MnO_2 was synthesized with K^+ ions occupying alternating layers of MnO_2. Because the spacing of the MnO_2 layers in δ-MnO_2 is affected by the size and occupancy of the interlayer cations, PXD is used to confirm the existence of K^+ ions in the sample (d). The cation site, X, is typically observed in a stoichiometric X:Mn ratio of approximately 0.2, i.e., $K_{0.2}MnO_2$ for both α and δ-MnO_2. The charge is balanced by Mn^{3+} sites within the MnO_6 subunits, yielding a net average oxidation state for the Mn at slightly less than 4+. The full range of occupancy variations is not explored further, because the cation sites are exchangeable, structurally irrelevant in the case of α-MnO_2 and inactive in redox cycling.

dx.doi.org/10.1021/ja310286h | J. Am. Chem. Soc. 2013, 135, 3494−3501

In contrast, the occupancy of A site vacancies of the delithiated spinel λ-MnO_2 does have a minimal structural effect and are observable by PXD. Both $LiMn_2O_4$ and its delithiated product, λ-MnO_2 (Figure 2e,f), form the spinel structure. However, delithiation is not a complete reaction and yields a compound with a stoichiometry of $Li_{0.2}Mn_2O_4$ abbreviated as λ-MnO_2 in agreement with the literature.[33] The diffraction pattern for λ-MnO_2 shifts to slightly higher angles (~3%) associated with delithiation and contraction of the cubic unit cell (Mn_4O_4 replicas), as previously reported.[6]

$LiMn_2O_4$, Mn_3O_4, Mn_2O_3 are highly stable, thermodynamically favored structures with only one accessible polymorph. The distorted spinel Mn_3O_4 (Figure 2h) possesses a unique diffraction pattern containing peaks representative of the spinel structure ($LiMn_2O_4$, Figure 2f) indicating a spinel unit with lower symmetry. The Mn_2O_3 structure (Figure 2g) is a pure material identical with that in the ICDD database.

Particle imaging by SEM of the monophasic structures reveal a range of particle sizes of morphology and facets and polycrystalline nature. No consistent correlation of catalytic activity exclusively with crystal morphology was evident across the 8 samples. Nanorod structures of various diameters were observed for β-MnO_2, α-MnO_2, and Mn_2O_3 (Figure 3a,c,g)

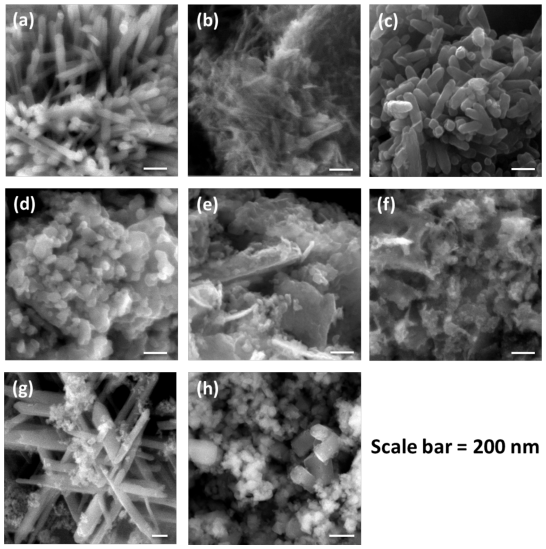

Figure 3. Scanning electron microscope (SEM) images of the eight Mn oxides reported herein: (a) β-MnO_2, (b) R-MnO_2, (c) α-MnO_2, (d) δ-MnO_2, (e) λ-MnO_2, (f) $LiMn_2O_4$, (g) Mn_2O_3, and (h) Mn_3O_4.

which includes both inactive and active polymorphs. In addition, the observed particle size distribution matches well with observed line broadening in the PXD patterns (uniform scan times). Specifically, the smallest particles, R-MnO_2 and λ-MnO_2 (Figure 3b,e) have broad features while the larger particles, β-MnO_2, Mn_2O_3, and Mn_3O_4 (Figure 3a,g,h) have sharp features. In addition to particle imaging, EDX measurements were performed to determine sample purity of active materials. In each material, no Ru, Fe, nor Ni were detected and between 0.5% and 0.8% Co was observed. XPS found no cobalt above its LOD = 1%. The Co impurity derives from the starting reagents and thus is present in all 8 Mn_xO_y materials. To quantitatively assess variations in particle size and morphology, BET surface area measurements were performed to allow for an accurate comparison of the materials based on the amount of actual surface Mn available for water oxidation (Figure S11). The BET surface areas (Table 1) vary between 17 m^2/g for Mn_2O_3 and 121 m^2/g for λ-MnO_2. Again, surface area alone did not account for the trend in catalytic activity in this study.

The electrochemical potential needed to drive water oxidation was provided by a commonly used one-electron photosensitizer, $Ru(bpy)_3^{2+}$ at 1.26 V versus NHE (η = 443 mV) with an electron acceptor, $Na_2S_2O_8$, in a 0.1 M sodium bicarbonate buffer at pH 7.0 (Supporting Information). Reaction conditions were held at pH 7 because at this pH the oxides are inert to dissolution, the photo-oxidant is stable, and this value maintains balance between the half reactions of water electrolysis.

Visible light-driven O_2 evolution in solution, normalized to surface area, is shown in Figure 4. The catalyst turnover frequencies (TOF) were determined from the slope of the dissolved O_2 concentration (Table 1). The slope was recorded in the linear region following the initial rise from 30 to 90 s of illumination with approximately 15% variance across triplicate experiments. All measurements were deliberately conducted with a fixed subsaturating concentration of photo-oxidant at constant light intensity that limited the TOF to less than its maximum achievable rates. The concentration dependence on Ru dye for λ-MnO_2 is given in Supporting Information (Figure S6). This protocol minimized photodegradation of the $Ru(bpy)_3^{2+/3+}$ dye on the time scale of the slope measurements.[6] As a result, the TOFs are only relative measures of rate. Three of the eight manganese oxides exhibit catalytic water oxidation activity with rates increasing: λ-$MnO_2 \ll Mn_3O_4 < Mn_2O_3$.

Following water oxidation, samples of the three active polymorphs were collected for XPS and HRTEM analysis. The total lack of post reaction amorphization observed by HRTEM on all surfaces of many nanoparticles surveyed reveals that the surface active sites are derived from the underlying crystal structures (Figure 5, Figures S7–S9). As the photooxidant is known to decompose, we were concerned about the possibility of forming RuO_2, itself a known water oxidizing catalyst. XPS measurements were performed on the collected nanoparticle after reaction and no Ru^{II}, Ru^{III}, nor Ru^{IV} signals were present in the spectra, indicating no detectable deposition of Ru on the catalyst (Figure S10).

DISCUSSION

Empirical correlations were first examined in an attempt to organize the data. Catalytic activity was observed for oxides of different stoichiometry (Mn:O = 1:2, 2:3, 3:4) and oxidation states (average 2.7 to 3.8). Only one of the five MnO_2 polymorphs exhibited catalytic activity, λ-MnO_2, which contains ~10% Mn^{3+} based on residual Li^+ content. Crystallite morphologies of both active materials and inactive materials include ordered nanorod structures (Figure 3a,c,g), as well as nonspecific nanoparticles (Figure 3b,d–f,h), revealing no identifiable correlation. Because average surface area differed for each material, catalytic activity was normalized to surface area. Among active catalysts, BET surface areas revealed a 7.5-fold range, with the highest (λ-MnO_2) and lowest (Mn_2O_3) surface area corresponding to the least and most active catalysts, contrary to typical correlations found within a single iso-structural family.

Many (but not all) of the manganese oxides described herein, have been studied individually by others, but typically under different conditions and without definitive structure validation (PXD), making direct comparisons difficult. Mn_2O_3 has been

dx.doi.org/10.1021/ja310286h | J. Am. Chem. Soc. 2013, 135, 3494–3501

Table 1. TOF and Selected Structural Parameters

Mn oxide	TOF[a,b] s^{-1}	BET $m^2\ g^{-1}$	TOF (surface) μmol $O_2\ m^{-2}\ s^{-1}$	avg. Mn−Mn distance, Å (edge-sharing octahedra)	avg. Mn−O distance, Å [oxygen coordination geometry][c,d]
(g) Mn_2O_3 (bixbyite)	3.7×10^{-4}	16.27	0.29	3.111	2.033 [μ_4 (*tet*)]
(h) Mn_3O_4 (hausmannite)	1.6×10^{-4}	27.22	0.068	3.042	2.026 [μ_4 (*tet*)]; 2.125 [μ_4 (*sq pln*)]; 2.1556 [μ_5 (*sq py*)]
(e) λ-MnO_2 (spinel)	5.5×10^{-5}	121.1	0.0078	2.821	1.962 [μ_3 (*tet*)]
(f) $LiMn_2O_4$ (spinel)	<LOD	24.5	<LOD	2.909	1.956 [μ_4 (*tet*)]
(c) α-MnO_2[e] (cryptomelane-type)	<LOD	74.58	<LOD	2.902	1.925 [μ_3 (*tet*)]; 1.886 [μ_3 (*tr pln*)]
(d) δ-MnO_2 (birnessite)	<LOD	17.88	<LOD	2.897	1.936 [μ_3 (*tet*)]
(a) β-MnO_2 (pyrosulite)	<LOD	14.92	<LOD	2.876	1.888 [μ_3 (*tr pln*)]
(b) R-MnO_2 (ramdsellite)	<LOD	89.27	<LOD	2.864	1.893 [μ_3 (*tet*)]; 1.904 [μ_3 (*tr pln*)]

[a]All TOF measured in 0.1 M $NaHCO_3$ pH 7; LOD = 0.05 nmol $O_2\ s^{-1}$. [b]Limited by photo-oxidant concentration (see text). [c]μ_N = oxygen with Mn coordination number *N*. [d](tet) = tetrahedral-like; (sq pln) = square planar-like; (sq) = square pyramidal-like; (tr pln) = trigonal planar-like. [e]α-MnO_2 was synthesized with and without K^+ ions and both were inactive (Supporting Information).

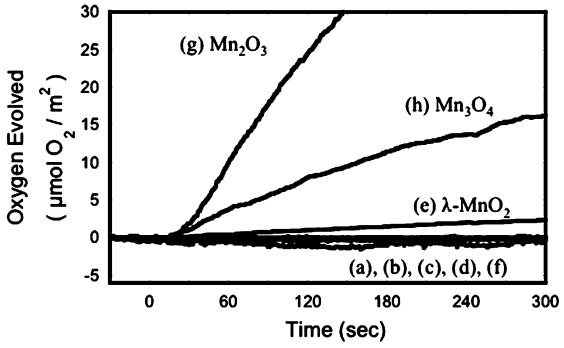

Figure 4. Dissolved O_2 concentration measured by Clark electrode at 23 °C, pH 7.0 for (a) β-MnO_2, (b) R-MnO_2, (c) α-MnO_2 (d) δ-MnO_2, (e) λ-MnO_2, (f) $LiMn_2O_4$, (g) Mn_2O_3, and (h) Mn_3O_4, normalized to total surface area. Illumination begins at time t = 0. Conditions: 0.5 mM $Ru(bpy)_3^{2+}$, 10 mM $Na_2S_2O_8$, and 250 ppm catalyst at pH 7.0.

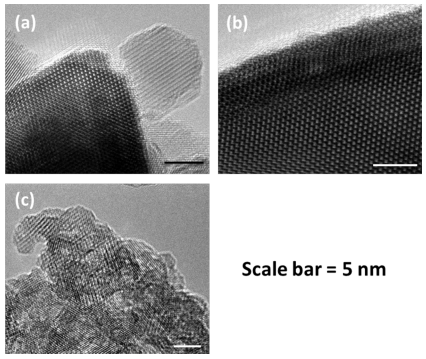

Figure 5. High-resolution transmission electron microscope (HRTEM) images of the three active water oxidation Mn oxides post reaction: (a) Mn_3O_4, (b) Mn_2O_3, (c) λ-MnO_2. See Supporting Information for survey.

studied numerous times as a water oxidation catalyst.[2,21] In early work, the activity was measured on micrometer sized Mn_2O_3 with a similar Ru photoassay and yielded a 3-fold higher initial rate when normalized to surface area (0.96 μmol $O_2\ m^{-2}\ s^{-1}$).[1] This difference likely arises from our use of subsaturating photo-oxidant concentration to facilitate unbiased comparisons herein. More recently in a manuscript on $CaMn_2O_4{\cdot}H_2O$ as a water oxidation catalyst, Mn_2O_3 was tested using the same Ru photoassay and it was reported to be much lower than the subject of the manuscript.[21] However, BET surface area measurements, reported in that same paper, reveal that Mn_2O_3 is in fact a significantly better catalyst than $CaMn_2O_4{\cdot}H_2O$ when normalized to surface area (0.26 vs 0.013 μmol $O_2\ m^{-2}\ s^{-1}$). Furthermore, the TOF reported for Mn_2O_3 corresponds well with the value reported in Table 1.

Although Mn_3O_4 is a well-known compound, there are no published reports attributing catalysis of water oxidation. However, Jiao and Frei detail water oxidation by manganese oxide nanoclusters grown within channels of a mesoporous silica.[18] These nanoclusters exhibit a range of oxidation states (determined from Mn XANES) that were fitted to an assumed mixture of Mn_3O_4 and Mn_2O_3. The specific catalytic activities of these composite nanoclusters are 16 μmol $O_2\ m^{-2}\ s^{-1}$ (for the Mn_3O_4-like sample) and 24 μmol $O_2\ m^{-2}\ s^{-1}$ (for the Mn_2O_3-like sample), determined with a similar Ru photoassay (Supporting Information). The reported activities are 10 times higher and were suggested to possibly arise from the higher intrinsic proton conductivity of mesoporous silica.[18] Despite the large difference in rates, the Mn_2O_3-like sample exhibits a corresponding higher rate than the Mn_3O_4-like sample, which we note follows the same trend observed herein.

Among the five MnO_2 polymorphs, several have been reported previously to be active water oxidation catalysts,[6,19,23] although structural characterization and purity considerations were incomplete or absent in most cases. By contrast, only one of these reported catalysts as synthesized herein was active in our hands. We reported earlier the synthetic λ-MnO_2 material to be an active catalyst,[6] and now include new data obtained for this manuscript with surface area normalization that enables direct comparisons.

In contrast to our results, both β-MnO_2 and α-MnO_2 have been reported to be active catalysts using a similar Ru photoassay.[23] Interestingly, our β-MnO_2 synthetic procedure, taken from the same source reference, yielded material with initially undetected Mn_2O_3 impurity that was revealed only upon improving the sensitivity of the PXD with much longer integration times (Figure S3). This impure material produced significant amount of O_2 (0.04 μmol $O_2\ m^{-2}\ s^{-1}$) that was attributable entirely to the Mn_2O_3 impurity quantified by PXD. Our rate for this impure material corresponds well with the value reported for "β-MnO_2" (0.02 μmol $O_2\ m^{-2}\ s^{-1}$).[23] Subsequently, we devised an alternative synthesis which removed the Mn_2O_3 impurity below our PXD detection limit (<3%) (Figure S3) and this β-MnO_2 yielded no catalytic activity. While structural assignment of β-MnO_2 as the major phase is accurate in reference 23, the low resolution PXD does

dx.doi.org/10.1021/ja310286h | J. Am. Chem. Soc. 2013, 135, 3494−3501

not rule out Mn_2O_3 impurity sufficient to account for all of the catalytic activity.

The same report describes the synthesis of α-MnO_2 nanoparticles with similarly lower resolution PXD, and also claiming a low level of water oxidation activity (0.014 μmol O_2 m^{-2} s^{-1}) that was not observed in our synthesized material.[19,23] As the occupancy of the cation sites within the 2 × 2 tunnel structure (Figure 1a) of α-MnO_2 is undetectable by PXD, we prepared both α-MnO_2 with K^+ in the cation sites as described above, and an alternative synthesis method that produces empty cation sites occupied by water[35] (Supporting Information). This form of α-MnO_2 is also structurally well-defined (Figure S4). Both materials exhibit no measurable activity (Table 1 (a) and Supporting Information).

Among the inactive materials, only R-MnO_2 lacks previous reports exploring catalytic water oxidation. We previously reported that spinel $LiMn_2O_4$ is catalytically inactive in water oxidation at all particle sizes examined (50−5000 nm).[6] However, topotactic removal of Li^+ yields catalytically active λ-MnO_2, which retains the cubic lattice structure. The cubic Mn_4O_4 core of this spinel polymorph provides a reactive template for catalyzing water oxidation, provided the A site cations are removed. We postulate that the added lattice flexibility arising from lowering the coordination number to three of the tetrahedral O atoms is essential for catalysis. This conclusion is reinforced by the example of $LiCoO_2$, which forms both cubic (3D) and layered (2D) polymorphs. Only the cubic polymorph, possessing cubical Co_4O_4 units and labile Li^+ cations that dissociate in solution, was shown to catalyze water oxidation.[7]

Recent reports have appeared of catalytic water oxidation from electrodeposited films of manganese oxide that were characterized by Mn EXAFS as containing exclusively 2D layered structures collectively called "birnessites" similar to δ-MnO_2.[36,37] However, because these disordered films are compositionally heterogeneous (being prepared from various Mn complexes), form from solutions at room temperature, and lack long-range order, we seriously doubt if they could be designated as a single structural polymorph of manganese oxide as claimed. These reports do not consider contamination by other polymorphs than δ-MnO_2. The eight Mn oxides reported herein are structurally difficult to distinguish by Mn EXAFS, as they differ only in terms of packing of similar MnO_6 octahedra (Figure 1). We found that only high resolution PXRD was able to definitively distinguish these structure types. While the literature contains many reports of structurally ill-defined Mn oxides that are referred to as "birnessite-like," solely on the basis of their major component, true δ-MnO_2 is a class of well-defined 2D layered phases with distinct crystal structure and layer separation, which depends upon the occupancy of the interstitial cation layer. Our results showing no activity from authentic δ-MnO_2 agree with a previous study of nanoparticles of δ-MnO_2 using a similar Ru photoassay that found no catalytic activity.[19]

Another report of electrodeposited manganese oxide films extended this approach to show that two types of films can be formed based on Mn EXAFS analysis, but only one of them is active catalytically.[20] Zaharieva et al. reported that the most active films contain more mono-μ-oxo bridged (corner-shared) MnO_6 octahedra (longer 3.45 Å Mn−Mn) and fewer di-μ-oxo bridged (edge-shared) octahedra (shorter 2.86 Å Mn−Mn) in the active material. The authors conclude that a higher fraction of longer Mn−O−Mn bridges is indicative of a more disordered structure, which they postulated as necessary for water oxidation.[20]

While the catalytic site for water oxidation must be on the aqueous exposed surface, our results show convincingly that the underlying structure is a critical determinant for the existence of surface active sites on nanocrystalline manganese oxides. While no detailed knowledge is available identifying the catalytic sites on the surface, the HRTEM data show definitively the surface is atomically ordered and necessarily resembles the underlying crystal structure. Therefore, the atomic structure of each bulk material is a logical starting point to search for correlations with catalytic rate. We examined the crystallographic parameters of the eight manganese oxides tested with specific focus on Mn−O bond lengths, the intermanganese (Mn−Mn) distances, and the Mn and O atom coordination number and geometry (Table 1). Only oxygen polyhedra coordinated by three or four Mn in edge-sharing octahedra were considered in calculating the Mn−Mn distances.

A comparison of first shell Mn−Mn distances averaged over all Mn ions (ignoring oxidation states) versus the O_2 TOF reveals no consistent trend (Table S1). However, when restricted to the edge-sharing MnO_6 octrahedra (includes only Mn^{III} and Mn^{IV}, but excludes Mn^{II}), a correlation favoring longer Mn−Mn distances is revealed, Figure 6 and Table 1

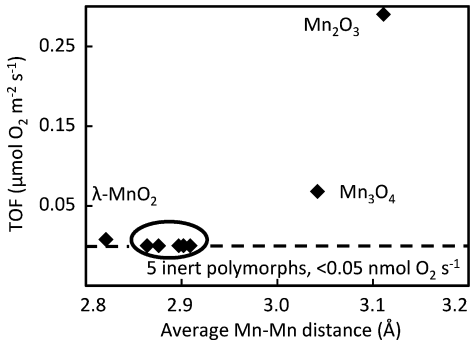

Figure 6. Comparison of surface area normalized TOF to the average Mn−Mn distance from Table 1 revealing the observed relation between longer Mn−Mn distances within the crystal structure and water oxidation activity.

(column 5 in g, h and e). These longer Mn−Mn distances represent bonding arrangements in which the oxygen atoms must be more weakly bonded. The exception, λ-MnO_2, is an interesting case of a low activity material that is a nonequilibrium phase of MnO_2 formed from $LiMn_2O_4$ with an open coordination site that potentially allows more flexibility. Although it has shorter intermanganese separation, the oxygen atoms - previously tetrahedrally bound to the Li and 3 Mn atoms by four sp^3 hybrid bonds - lose one bond. These corner μ_3-oxos (i.e., oxygens in OMn_3 environment) retain three sp^3 hybrid bonds that are longer and weaker than achievable in other geometries. (Table 1). Indeed, inspection of the Mn−O bond lengths (Table 1, column 6) reveals that all catalytically active oxides possess longer Mn−O distances in edge-sharing octahedra.

A series of crystalline perovskites, composition ABO_3, composed of 12 examples of variable A and B type and content, were shown to exhibit water oxidation activity that tracks closely with the electron population of the d orbitals of the B atom.[9] Specifically, B atoms with about 1.2 electrons in the antibonding e_g symmetry orbital were shown to exhibit the

dx.doi.org/10.1021/ja310286h | J. Am. Chem. Soc. 2013, 135, 3494−3501

lowest overpotential (highest activity), while those with fewer or more were less active. This differs with the trends we observe across structurally different Mn oxide polymorphs. Notably, although the e_g^1 occupation of Mn^{III} present in (distorted) cubic phases (bixbyite, hausmanite, spinels) of Mn_2O_3 (100%), Mn_3O_4 (67%) and λ-MnO_2 (<10%, based on residual Li^+ content) correlates well with their relative O_2 evolution activities, the spinel $LiMn_2O_4$ with 50% Mn^{3+} is inactive.

CONCLUSIONS

Catalytic water oxidation activity varies appreciably among the crystalline Mn oxides and is favored by specific structure/bonding types that were not adequately identified prior to this work. By devising synthesis procedures that produce pure polymorphs and accounting for variables that influence water oxidation activity (surface area, overpotential, buffer), we are able to focus on the intrinsic structural/bonding parameters of the underlying lattice that affect catalysis. The most active materials (Mn_2O_3, and Mn_3O_4) all possess $Mn^{III}(d^4)$ in edge-sharing octahedra with longer (Jahn−Teller distorted) Mn−O bonds than Mn^{IV} (d^3). Mn^{III} forms weaker Mn−O bonds due to occupation of the *antibonding* e_g orbital. We hypothesize that Mn^{III}−O in edge sharing octahedra at the surface are more reactive catalytically due to these weaker, more flexible bonds. In contrast, the MnO_2 polymorphs with shorter and stronger Mn^{IV}−O bonds are more stable, and do not foster the high oxidation potential and flexibility needed for catalysis of O_2 formation. Only if the MnO_2 lattice is further weakened and made more flexible as in λ-MnO_2, does low-level catalytic water oxidation activity appear.

In future studies, we aim to examine electro-catalytic water oxidation with these materials, which allows investigation of lifetimes under variable overpotentials and pH.

ASSOCIATED CONTENT

Supporting Information

Synthesis procedures for α-MnO_2 (k); experimental details for oxygen evolution procedure; procedures for calculating bond distances; additional HRTEM images of post reaction active materials. This material is available free of charge via the Internet at http://pubs.acs.org.

AUTHOR INFORMATION

Corresponding Author

dismukes@rci.rutgers.edu, martha@chem.rutgers.edu

Notes

The authors declare no competing financial interest.

ACKNOWLEDGMENTS

We thank the following funding sources: AFOSR grant FA9550-11-1-0231 (G.C.D.), Rutgers University for partial fellowship support (D.M.R.), DOE Office of Basic energy Sciences grant DE-FG02-10ER16195 for partial fellowship (G.G.), NSF-DMR grant 0966829 (M.G.) and partial fellowship (Y.B.G.), summer fellowship from the Lawrenceville School, Lawrenceville, NJ (M.M.). We thank Dr. Gennady Ananyev for instrumentation support, Prof. Gerhard Swiegers and Dr. Clyde Cady for discussions. We thank Dr. Nan Yao at the Princeton Institute for Science and Technology of Materials (PRISM) for imaging analysis.

REFERENCES

(1) Jensen, J. O.; Bandur, V.; Bjerrum, N. J.; Jensen, S. H.; Ebbesen, S.; Mogensen, M.; Tophoj, N.; Yde, L.; *Pre-Investigation of Water Electrolysis*; Technical University of Denmark (DTU), Riso National Laboratory, and DONG Energy: Denmark, 2008. http://130.226.56.153/rispubl/NEI/NEI-DK-5057.pdf (accessed Dec 20, 2012).
(2) Harriman, A.; Pickering, I. J.; Thomas, J. M.; Christensen, P. A. *J. Chem. Soc., Faraday Trans.* **1988**, *84*, 2795.
(3) Luneva, N. P.; Shafirovich, V. Y.; Shilov, A. E. *J. Mol. Catal.* **1989**, *52*, 49.
(4) Tributsch, H. *Electrochim. Acta* **2007**, *52*, 2302.
(5) Youngblood, W. J.; Lee, S.-H. A.; Kobayashi, Y.; Hernandez-Pagan, E. A.; Hoertz, P. G.; Moore, T. A.; Moore, A. L.; Gust, D.; Mallouk, T. E. *J. Am. Chem. Soc.* **2009**, *131*, 926.
(6) Robinson, D. M.; Go, Y. B.; Greenblatt, M.; Dismukes, G. C. *J. Am. Chem. Soc.* **2010**, *132*, 11467.
(7) Gardner, G. P.; Go, Y. B.; Robinson, D. M.; Smith, P. F.; Hadermann, J.; Abakumov, A.; Greenblatt, M.; Dismukes, G. C. *Angew. Chem., Int. Ed.* **2012**, *51*, 1616.
(8) Esswein, A. J.; McMurdo, M. J.; Ross, P. N.; Bell, A. T.; Tilley, T. D. *J. Phys. Chem. C* **2009**, *113*, 15068.
(9) Suntivich, J.; May, K. J.; Gasteiger, H. A.; Goodenough, J. B.; Shao-Horn, Y. *Science* **2011**, *334*, 1383.
(10) Jiao, F.; Frei, H. *Angew. Chem., Int. Ed.* **2009**, *48*, 1841.
(11) Yang, J.; Li, J.; Lin, H.; Yang, X.; Tong, X.; Guo, G. *J. App. Electrochem.* **2006**, *36*, 945.
(12) Brimblecombe, R.; Swiegers, G. F.; Dismukes, G. C.; Spiccia, S. *Angew. Chem., Int. Ed.* **2008**, *47*, 7335.
(13) McCool, N. S.; Robinson, D. M.; Sheats, J. E.; Dismukes, G. C. *J. Am. Chem. Soc.* **2011**, *133*, 11446.
(14) El Wakkad, S. E. S.; Hickling, A. *Trans. Faraday Soc.* **1950**, 46.
(15) Suzuki, O.; Takahashi, M.; Fukunaga, T.; Kuboyama, J. U.S. Patent. 3,399,966, Sep 3, 1968.
(16) Brunschwig, B. S.; Chou, M. H.; Creutz, C.; Ghosh, P.; Sutin, N. *J. Am. Chem. Soc.* **1983**, *105*, 4832.
(17) Kanan, M. W.; Nocera, D. G. *Science* **2008**, *321*, 1072.
(18) Jiao, F.; Frei, H. *Chem. Commun.* **2010**, *46*, 2920.
(19) Iyer, A.; Del-Pilar, J.; King,Äôondu, C. K.; Kissel, E.; Garces, H. F.; Huang, H.; El-Sawy, A. M.; Dutta, P. K.; Suib, S. L. *J. Phys. Chem. C* **2012**, *10*, 6474.
(20) Zaharieva, I.; Dau, H. *Energy Environ. Sci.* **2012**, *3*, 2330.
(21) Najafpour, M. M.; Ehrenberg, T.; Wiechen, M.; Kurz, P. *Angew. Chem., Int. Ed.* **2010**, *49*, 2233.
(22) Post, J. E. *Proc. Natl. Acad. Sci. U.S.A.* **1999**, *96*, 3447.
(23) Boppana, V. B. R.; Jiao, F. *Chem. Commun.* **2011**, *47*, 8973.
(24) Takashima, T.; Hashimoto, K.; Nakamura, R. *J. Am. Chem. Soc.* **2011**, *134*, 1519.
(25) Wang, X.; Li, Y. *J. Am. Chem. Soc.* **2002**, *124*, 2880.
(26) Rossouw, M. H.; de Kock, A.; Liles, D. C.; Gummow, R. J.; Thackeray, M. M. *J. Mat. Chem* **1992**, *2*, 1211.
(27) Devaraj, S.; Munichandraiah, N. *J. Phys. Chem. C* **2008**, *112*, 4406.
(28) Ching, S.; Landrigan, J. A.; Jorgensen, M. L. *Chem. Mater.* **1995**, *7*, 1604.
(29) Lei, S.; Tang, K.; Fang, Z.; Liu, Q.; Zheng, H. *Mater. Lett.* **2006**, *60*, 53.
(30) Zhang, S.; Chen, Z.; Tan, S.; Wang, J.; Jin, S. *Nanostruct. Mater.* **1997**, *8*, 719.
(31) Gibot, P.; Laffont, L. *J. Solid State Chem.* **2007**, *180*, 695.
(32) Chabre, Y.; Pannetier, J. *Prog. Solid State Chem.* **1995**, *23*, 1.
(33) Hunter, J. C. *J. Solid State Chem.* **1981**, *39*, 142.
(34) Inorganic Crystal Structure Database (ICSD), FIZ Karlsruhe, 2012.
(35) Johnson, C. S.; Dees, D. W.; Mansuetto, M. F.; Thackeray, M. M.; Vissers, D. R.; Argyriou, D.; Loong, C. K.; Christensen, L. *J. Power Sources* **1997**, *68*, 570.
(36) Wiechen, M.; Zaharieva, I.; Dau, H.; Kurz, P. *Chem. Sci.* **2012**, *3*, 2330.

(37) Hocking, R. K.; Brimblecombe, R.; Chang, L.-Y.; Singh, A.; Cheah, M. H.; Glover, C.; Casey, W. H.; Spiccia, L. *Nat. Chem.* **2011**, *3*, 461.